Title
A Mechanistic Analysis of Phase Evolution and Hydrogen Storage Behavior in Nanocrystalline Mg(BH4)2 within Reduced Graphene Oxide

Journal
ACS Nano, 14(2)

ISSN
1936-0851

Authors
Jeong, Sohee
Heo, Tae Wook
Oktawiec, Julia
et al.

Publication Date
2020-02-25

DOI
10.1021/acsnano.9b07454

Peer reviewed

Title

Unveiling the mechanism of phase evolution and hydrogen storage behavior in nanocrystalline $Mg(BH_4)_2$ within reduced graphene oxide

Authors

Sohee Jeong[1], Tae Wook Heo[2], Julia Oktawiec[3,7], Rongpei Shi[2], ShinYoung Kang[2], James L. White[4], Andreas Schneemann[4], Edmond W. Zaia[1], Liwen F. Wan[2], Keith G. Ray[2], Yi-Sheng Liu[5], Vitalie Stavila[4], Jinghua Guo[5,6], Jeffrey R. Long[3,7,8], Brandon C. Wood[2], Jeffrey J. Urban[1*]

[1] The Molecular Foundry, Materials Sciences Division, Lawrence Berkeley National Laboratory, Berkeley, California 94720, USA

[2] Materials Science Division, Lawrence Livermore National Laboratory, Livermore, California 94550, USA

[3] Department of Chemistry, University of California, Berkeley, California 94720, USA

[4] Chemistry, Combustion, and Materials Science Center, Sandia National Laboratories, Livermore, California 94550, USA

[5] Advanced Light Source, Lawrence Berkeley National Laboratory, Berkeley, California 94720, USA

[6] Department of Chemistry and Biochemistry, University of California, Santa Cruz, California 95064, USA

[7] Materials Sciences Division, Lawrence Berkeley National Laboratory, Berkeley, California, 94720, USA

[8] Department of Chemical and Biomolecular Engineering, University of California, Berkeley, California, 94720, USA

Abstract

Magnesium borohydride ($Mg(BH_4)_2$, abbreviated here MBH) has received tremendous attention as a promising onboard hydrogen storage medium due to its excellent gravimetric and volumetric hydrogen storage capacities. While the polymorphs of MBH—alpha (α), beta (β), and gamma (γ)—have distinct properties, their synthetic homogeneity can be difficult to control, mainly due to their structural complexity and similar thermodynamic properties. Here, we describe an effective approach for obtaining pure polymorphic phases of MBH nanomaterials within a reduced graphene oxide support (abbreviated MBHg) under mild conditions (60–190 °C under mild vacuum, 2 Torr), starting from two distinct samples initially dried under Ar and vacuum. Specifically, we selectively synthesize the thermodynamically-stable α phase and metastable β phase from the γ-phase within the temperature range of 150–180 °C. The relevant underlying phase evolution mechanism is elucidated by theoretical thermodynamics and kinetic nucleation modeling. The resulting MBHg composites exhibit structural stability, resistance to oxidation, and partially reversible formation of diverse $[BH_4]^-$ species during de- and rehydrogenation processes, rendering them intriguing candidates for further optimization toward hydrogen storage applications.

Key words

Magnesium borohydride, hydrogen storage, phase evolution, thermodynamics, kinetic, reduced graphene oxide

Hydrogen is an earth-abundant, clean energy carrier that has the potential to reduce reliance on carbon-based energy sources, such as oil.[1-4] Metal borohydrides have attracted substantial interest as hydrogen storage media, due to their excellent theoretical hydrogen storage capacities and their potential to meet U.S. Department of Energy (DOE) requirements.[5-7] The prototypical example is $Mg(BH_4)_2$ (abbreviated MBH), which possesses a high gravimetric hydrogen content (14.9 wt %), high volumetric hydrogen density (147 kg/m^3), and a low enthalpy of formation (40 kJ/mol).[8,9] MBH is known to have an unusually large number of phase polymorphs and high structural complexity, with representative alpha (α), beta (β), and gamma (γ) phases that crystallize as hexagonal, orthorhombic, and cubic structures, respectively.[10] Known as the low-temperature phase, α-MBH can be transformed to the high-temperature β-MBH phase at ~180 °C. Theoretical studies have predicted that α-MBH has the potential to be a near-ideal hydrogen storage material within a low temperature and enthalpy range (35–54 kJ/mol H_2 at 20–75 °C)[11-15]. Likewise, the nanoporous polymorph γ-MBH possesses a high surface area (1160 m^2/g) and low material density (ρ = 0.55 g/cm^3), which allows it to absorb additional 0.8 H_2 molecules to the interior of the γ-MBH to form γ-MBH·0.8H_2 with a large hydrogen storage capacity of 17.4 wt %.[16,17] Based on experimental and theoretical studies, dehydrogenation of α- or γ-MBH upon heating generally results in an irreversible phase transformation to β- or β′- (disordered variant of β) MBH.[11-15, 17,18] Establishing an in-depth understanding of the dehydrogenation and rehydrogenation mechanisms of MBH is crucial to its further development as a candidate hydrogen storage material and accordingly requires isolation of each pure-phase polymorph. However, lack of synthetic homogeneity in synthesized MBH samples has been one challenge in developing this material to further technological maturity. Additionally, significant discrepancies exist among the theoretical predictions of phase expression, because the polymorphs have very similar thermodynamic properties (*e.g*., enthalpy of formation) and the relevant phases exhibit some unusually complex crystal structures.[19-22]

Polymorphs of MBH can be synthesized by mechanical milling, gas-solid reactions, and solution-based reactions,[10, 23-27] while the most widely used method is ball milling under either high temperature or a high pressure of H_2.[11, 28] These harsh preparation conditions, although effective, result in poor phase controllability. Moreover, these conditions are energy-intensive and susceptible to sample contamination from traces of the milling media. Alternative routes under relatively mild conditions have been developed that involve metathesis or Lewis acid-base reactions with ethereal solvents. However, the resulting products are often contaminated with byproduct salts, unsolvated compounds, and undesired phases.[8, 11, 29-31] For example, only the β phase can be readily obtained *via* the milder solution approach, because desolvation of the as-synthesized MBH/solvent complex typically requires high vacuum (< 10^{-3} mbar) and temperatures above the α to β phase transition (> 200 °C). Ultimately, it remains necessary to develop more mild synthetic strategies capable of yielding desired phase-pure MBH in a controlled fashion. Even though there are a few of previous examples in the literature which reported synthetic methods, most provided only one or two phases and focused on their structural analysis. [6, 16, 32]

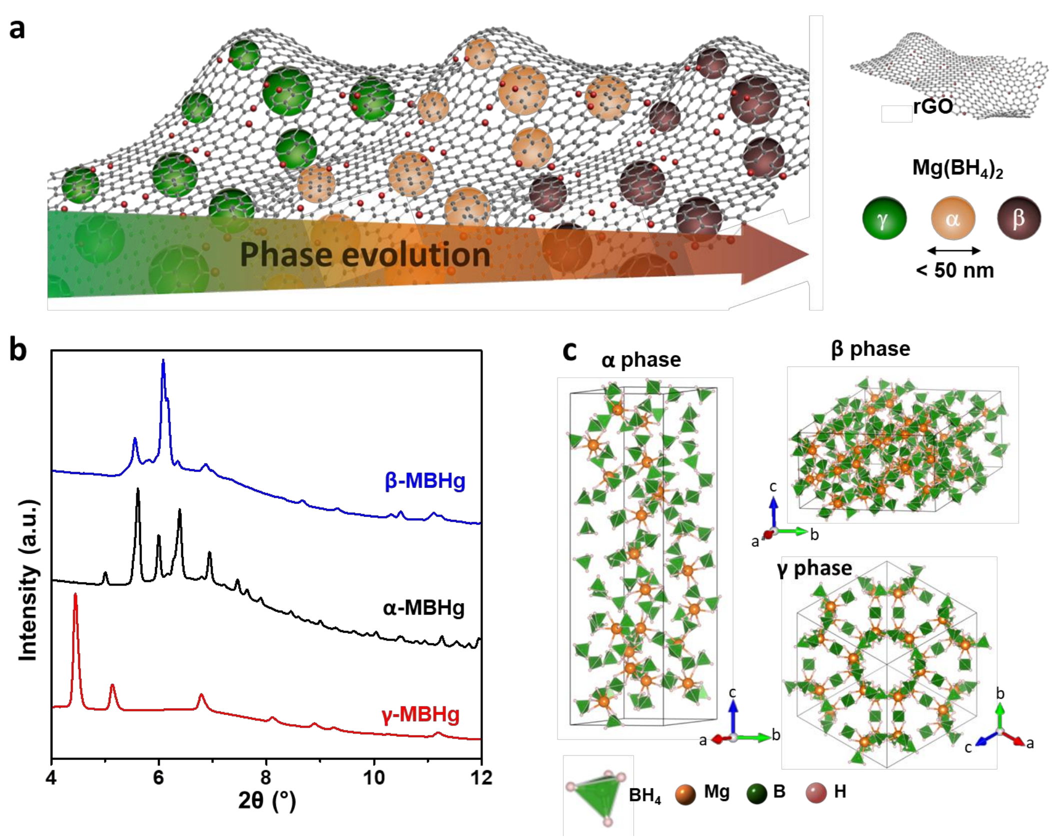

Figure 1. a) Schematic illustration of phase evolution in MBH supported by reduced graphene oxide (MBHg). b) Powder X-ray diffraction data of γ (red), α (black), and β (blue) phased of MBHg at room temperature (λ = 0.499316 Å). c) Structural models of the α, β and γ phases of MBH. Green, orange, and pink spheres represent Mg, B, and H atoms, respectively; $[BH_4]^-$ groups are depicted as green tetrahedra and unit cells are defined by solid gray lines.

Here, we utilize crystal phase evolution to generate pure α-, β-, and γ-MBH supported by atomically-thin reduced graphene oxide (rGO) nanomaterials (hereafter, MBHg) under mild conditions (Figure 1). We also use computational analysis to understand and predict the experimental conditions that yield selective polymorphic phases of MBH. Using kinetic nucleation models, we elucidate a plausible pathway toward the formation of the thermodynamically unfavorable β phase, and experimentally demonstrate thermodynamically favorable phase evolution from the γ to α phase in a temperature range of 150–180 °C, a result supported by our theoretical analysis. Evaluation of the hydrogen desorption and absorption performance of the resulting MBHg nanomaterials reveals that rGO acts as a protective barrier from O_2 and/or H_2O contamination and also a supporting matrix to provide environmental stability and nanoscale confinement upon H_2 cycling.[33] Finally, cycling experiments and calculations reveal that MBHg follows multiple reaction pathways and shows partially-reversible H_2 uptake.

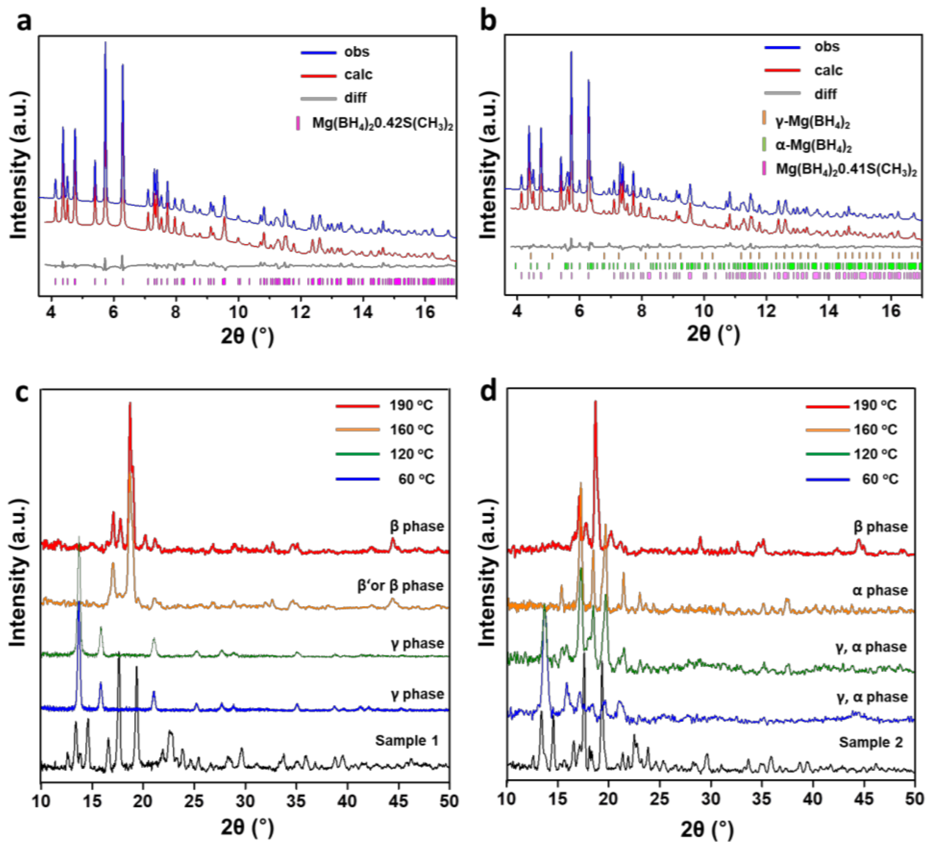

Figure 2. a,b) Powder X-ray diffraction patterns and refinement analysis of sample **1** (a) and sample **2** (b) at room temperature. Blue and red lines represent the observed and calculated diffraction patterns, respectively. The gray line represents the difference between observed and calculated patterns, and the pink, orange, and bright green vertical lines indicate calculated Bragg peak positions (λ = 0.499316 Å). c,d) Temperature-dependent phase expression in magnesium borohydride achieved by increasing the temperature of sample **1** (c) and sample **2** (d) from 60 to 120, 160, and 190 °C (λ = 1.54056 Å).

Results and Discussion

The MBHg nanomaterials were synthesized using a modification of a previously reported method for the synthesis of crystalline MBH in non-coordinating solvent.[34] Briefly, a suspension of rGO in toluene was added to a solution of $Mg(C_4H_9)_2$ in heptane. This mixture was diluted with toluene and stirred for 30 min before being added to 2 equiv of $BH_3{\cdot}S(CH_3)_2$ in toluene. The mixture was stirred overnight under Ar, which resulted in the formation of a gray precipitate. The solid was subsequently isolated and dried under vacuum for 3 min (sample **1**) or under Ar for 1 d (sample **2**, see Methods for full details). To better probe the structures and phase distribution present in **1** and **2**, we carried out Rietveld refinement analysis using synchrotron powder X-ray diffraction patterns collected on both samples at room temperature (Figure

2a,b). Sample **1** crystallizes with the formula $Mg(BH_4)_2{\cdot}0.42S(CH_3)_2$ (Supporting Information, Figure S1, Table S1) and features two Mg^{2+} environments—one in which the metal ion is tetrahedrally coordinated by four borohydride groups and one in which Mg^{2+} is at the center of a trigonal bipyramid formed by four BH_4^- and one $S(CH_3)_2$ ligand (Supporting Information, Figure S3). Interestingly, sample **2** was found to be a multiphase solid consisting of 79.6% $Mg(BH_4)_2{\cdot}0.41S(CH_3)_2$, 17% α phase (with average particle sizes of ~30 nm in diameter, as determined from powder X-ray diffraction data, Supporting Information, Figure S4), and 3.4% γ phase (see Supporting Information, Figure S2, Table S1). Thus, rapid drying under vacuum seems to favor the formation of a single phase, while multiple phases can be accessed under more gradual drying conditions at room temperature. Given the final composition of samples **1** and **2**, rapid drying also seems to remove toluene only, while slow drying also promotes evaporation of some dimethyl sulfide.

To monitor phase evolution with increasing temperature in samples **1** and **2**, we heat treated both samples at 60, 120, 160, and 190 °C under vacuum (2 Torr). Sample **1** begins to directly form the γ phase below 60 °C, with complete transformation between 60 and 120 °C. Subsequently, the sample begins to transform to the β or β′ phase above 120 °C (Figure 2c), with complete transformation between 160 and 190 °C. For sample **2**, the α phase dominates with increasing temperature and is the exclusive phase present at 160 °C (Figure 2d). Interestingly, to our knowledge there have been no reports of transformation from the γ to α phase, although the α phase is predicted to be more thermodynamically favorable than β phase between 150 and 180 °C, while the γ to β (or β') transition has been widely observed in many experimental studies.[17,18, 20] Ultimately, these results indicate that we are able to selectively realize both thermodynamically favorable (α phase) and thermodynamically unfavorable (β or β′ phase) phase evolution in our system. Interestingly, MBH without rGO shows the similar phase evolution (Supporting Information, Figure S5).

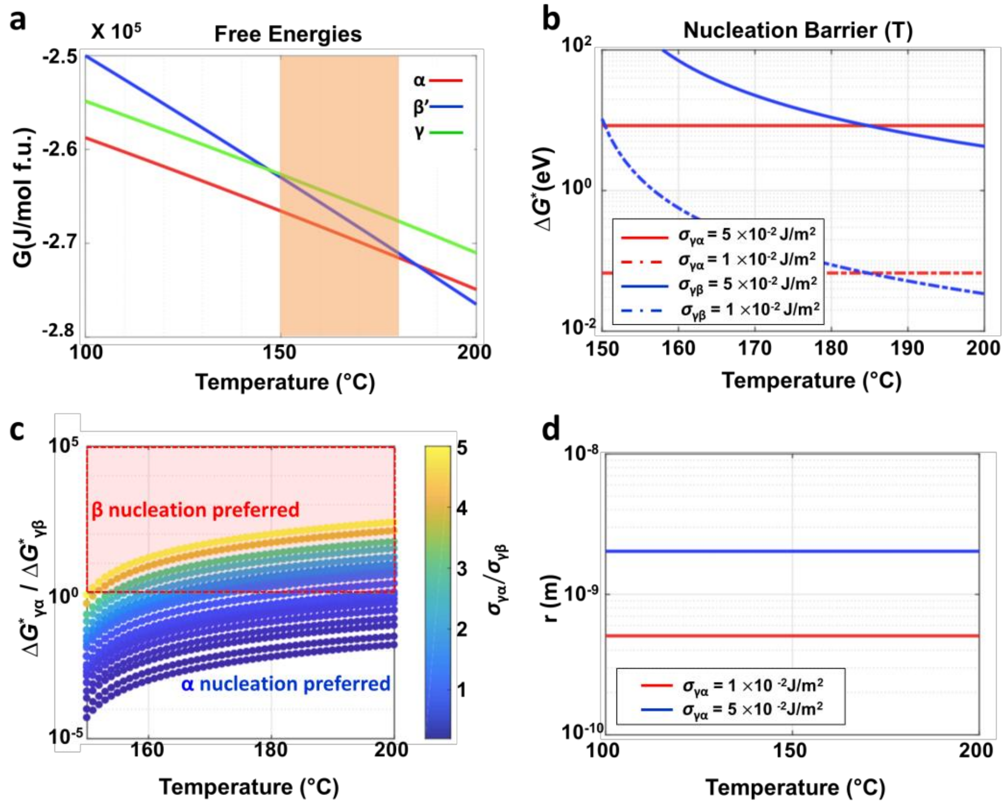

Figure 3. a) Free energy curves for relevant polymorphic MBH phases. b) Computed nucleation barriers for γ → α and γ → β transformations for different values of the interfacial energy (σ) between phases. c) Computed ratio of α and β nucleation barriers for sampled ratios of the corresponding interfacial energies. d) Computed critical nuclei sizes for the γ → α phase transformation.

To explain the experimental phase evolution observed with varying temperature, we first examined the relative thermodynamic stabilities of relevant MBH phases. Figure 3a shows the Gibbs free energies of the relevant α, β (or β′), and γ phases, which are informed by the available CALPHAD (CALculation of PHAse Diagrams) thermodynamic database and known phase transition temperatures[20] (see Methods for the detail). Our thermodynamic analysis indicates that the α phase should be most stable within the considered temperature range (150–180 °C). Thus, the transformation of sample **1** to the β phase at elevated temperatures cannot be explained by thermodynamics alone. Instead, we invoke phase nucleation kinetics to elucidate the observed phase transformations behavior. In particular, we hypothesized that for sample **1**, nucleation of the α phase in the γ phase is penalized compared to β phase nucleation.

To test this hypothesis, we employed classical phase nucleation theory[35] to compute and compare the nucleation barriers for γ → α and γ → β transformations, using the thermodynamic driving forces obtained from the free energy calculations in Figure 3a. Note that a key ingredient in the formulation of these nucleation barriers is the α/γ or β/γ heterogeneous interfacial energy, which is challenging to measure directly or accurately compute, due to the lack of detailed information about the interfacial structures at the atomistic and mesoscopic scales. Instead of direct evaluation, we chose reasonable estimates of MBH interfacial energies based on the antiphase boundary or stacking fault energy calculated using DFT (Methods for the calculation details). Note that this approach assumes that all relevant polymorphic phase boundaries are structurally similar to twin or domain boundaries, which is reasonable given the similarity of local coordination motifs among the structures. In Figure 3b, we explored the phase nucleation behavior as a function of temperature by selecting two reasonable values of interfacial energies (denoted σ) within the relevant temperature range of interest highlighted by the pale orange region in Figure 3a. These values represent our best estimates of the probable limits of interfacial energies based on the DFT calculations, assuming either a coherent interface (0.05 J/m^2) or a semi-coherent interface (0.01 J/m^2).

Our results indicate two major characteristics for the nucleation barriers: (1) the nucleation barrier for the $\gamma \rightarrow \beta$ transformation is more sensitive to temperature than its $\gamma \rightarrow \alpha$ counterpart—a consequence of the larger entropy of the β phase—and (2) both computed nucleation barriers are highly sensitive to the associated interfacial energies. Importantly, these calculations demonstrate that, depending on the specific values of the interfacial energies, the β phase nucleation barrier could be much smaller than the α phase nucleation barrier within the relevant temperature range of 150–180 °C (for instance, compare the red solid and blue dashed curves, Figure 3b). This smaller barrier would lead to kinetic preference for the formation of the β phase within the γ phase and notably, once the beta phase is formed it stays as metastable phase within these temperature ranges (Supporting Information, Figure S6), despite the thermodynamic stability of the α phase observed for sample **1**.

Next, we explored the full range (0.01 to 0.05 J/m^2) of probable interfacial energy magnitudes to sample all possible conditions that lead to preferred β phase nucleation at the thermodynamic conditions in our study. Figure 3c includes the computed nucleation barrier ratios for the $\gamma \rightarrow \alpha$ and $\gamma \rightarrow \beta$ phase transformations for all sampled interfacial energies, indicating the kinetic preference for phase formation as a function of temperature. We emphasize that there are a large number of conditions for which we compute a propensity for β phase nucleation ($\Delta G^*_{\gamma\alpha} / \Delta G^*_{\gamma\beta} > 1$) within the temperature range of interest (150–180 °C) despite the thermodynamic stability of the α phase; these conditions are met whenever the interfacial energy ratio ($\sigma_{\gamma\alpha}/\sigma_{\gamma\beta}$) exceeds critical values. Therefore, we hypothesize that the phase boundaries in **1** satisfy these conditions under the synthesis temperatures used here, leading to β phase nucleation. Although we do not know the exact value of $\sigma_{\gamma\alpha}/\sigma_{\gamma\beta}$, we emphasize that this claim is reasonable given the larger unit cell and higher relative entropy of the β phase compared with the α phase, which offers more internal degrees of freedom for atomic reconfiguration at the interface with γ.

For sample **2**, the pre-existing α phase plays a key role in determining the phase behavior. Since the α phase is thermodynamically preferred within the explored temperature range, the characterized α phase growth can be easily explained if the particle size of the pre-existing α phase is larger than the critical nucleus size of the α phase in the γ phase, as computed from phase nucleation theory. Figure 3d shows the estimated critical nucleus sizes for our estimates of the two representative limits of relevant interfacial energies (representing coherent and semi-coherent assumptions). The probable critical nucleus size is < 10 nm, while the experimental volume-weighted average α particle size is ~30 nm (Figure 3d, determined from analysis of powder X-ray diffraction data) and ~15 nm (Supporting Information, Figure S7, determined from analysis of TEM data). Therefore, this result indicates that the pre-existing α phase is well above the critical nucleus size and should grow according to its preferred thermodynamic stability. Interestingly, this result implies that the α phase will continue to grow as long as γ/α interface maintains coherent or semi-coherent behavior, which is a reasonable assumption during evolution for nanoscale particles.[36] As a result, the differences between samples **1** and **2** appear to reflect the competition between nucleation kinetics and thermodynamics, as determined in part by the existence or lack of key presursor phases during syntheis.

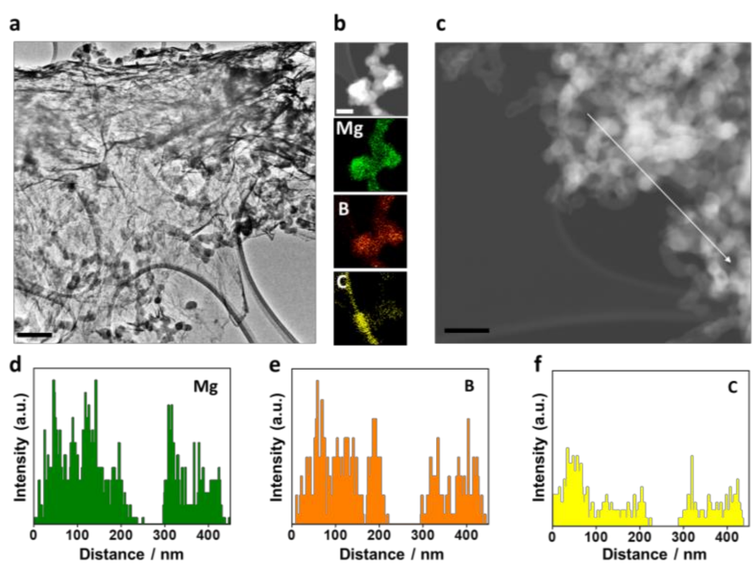

Figure 4. a) TEM images of γ-MBHg and (b) energy dispersive X-ray spectroscopy (EDS) mapping of γ-MBHg for Mg, B, and C, respectively. c) STEM image and (d-f) EDS line mapping for Mg, B, and C of corresponding to the white line in part (c). Scale bar: 100 nm

Transmission electron microscopy (TEM), scanning transmission electron microscopy (STEM), and powder X-ray diffraction were used to characterize samples of γ, β, and α-MBHg obtained through phase evolution. The nanoparticle diameter was found to be < 50 nm based on TEM images (Figure 4a, Supporting Information, S8, and S9), and average crystallite sizes were approximately 30, 31, and 28 nm for γ, α, and β phases, respectively, as estimated by Scherrer analysis of powder X-ray diffraction patterns. (Supporting Information, Tables S2, S3, and S4). Elemental analysis and line mapping confirmed that as-synthesized MBHg nanomaterials are composed of Mg, B, and C elements and provided further support for the characterized nanosized dimension of MBHg (Figure 4, Supporting Information, Figure S8, and S9). The amount of rGO in the MBHg is 1.0 – 4.0 wt% overall.

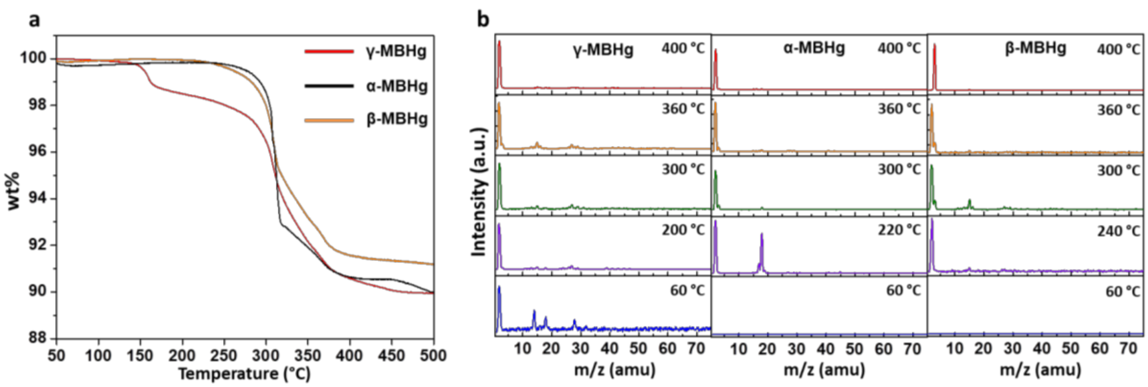

Figure 5. a) TGA traces of α-MBHg, β-MBHg and γ-MBHg in black, orange and red respectively. b) Mass spectra of α-MBHg, β-MBHg and γ-MBHg recorded at different temperatures.

The hydrogen desorption properties of MBHg nanohydrides were tested using thermogravimetric analysis (TGA), Mass spectrometry, and a Sieverts-type instrument at 390 °C and an initial pressure of 0 bar (Figure 5 and Supporting Information, Figure S10-S13). TGA analysis of the materials shows that all three materials have distinct dehydrogenation profiles (Figure 5a). While α-MBHg and β-MBHg show a one-step weight loss profile (onset at 270 and 250 °C respectively), γ-MBHg has a two-steps decomposition profile, with onsets of the weight loss at 150 and 270 °C. The mass spectra recorded at lower temperatures suggest that the major fraction of the released weight is hydrogen. Interestingly, this weight loss step is located in the same region as the phase transition of γ-MBHg to β-MBHg (Figure 2c). A total weight loss of 10.0, 8.8 and 10.1 wt% is observed for α-MBHg, β-MBHg and γ-MBHg, respectively. Notably, 1.3 wt% of the weight loss in γ-MBHg are attributed to the first release step. The observed weight loss of the MBHg is close to the expected weight loss if only clean H_2 is released from the materials. Additionally, residual gas analysis mass spectrometry was performed on the materials, to survey the composition of the released gas at different temperatures in range of 60 °C to 400 °C (Figure

5b and Supporting Information, S10-S12). Noteworthy, the materials release clean hydrogen over the whole temperature range. Some exceptions include the appearance of masses representing H_2O, which we ascribe to water adsorbed on the walls of the used stainless steel reactor or on the steel tubing which is exposed to air during the sample mounting. Furthermore, some minor signals might represent slight decomposition of the materials at elevated temperatures, *i.e*. the signals at 14-15 and 27 can be attributed to CH_x fragments, CO as well as minor amounts of B_2H_6. Under the assumption that gas coming off from MBHg nanohydrides is only hydrogen the hydrogen capacities determined *via* Sieverts measurements, from the first desorption were 11.2, 10.3, and 9.9 wt % H for the γ, β, and α phase, respectively (Supporting Information, Figure S13a). Noteworthy, these values are of similar magnitude with the values obtained from TGA. Subsequent desorption experiments were performed at 390 °C after rehydrogenation at 400 °C and 700 bar, constituting cycles 2 and 3. The hydrogen capacity of γ-MBHg decreased to ~3.5 and ~ 1.5 wt % H in the second and third cycles (Supporting Information, Figure S13b), suggesting that a low amount of H_2 is readsorbed after the first dehydrogenation or that residual hydrogen is still present in the form of amorphous borane or Mg-polyboranes (*e.g*., $MgB_{12}H_{12}$), which are known to be stable during cycling. The α- and β-MBHg phases exhibited similar behavior to γ-MBHg (Supporting Information, Figure S13c,d). Although we only observe partial reversibility for all three phases over three cycles and an apparently low capacity for H_2 readsorption, further analysis revealed the cycling potential for these composites (see below).

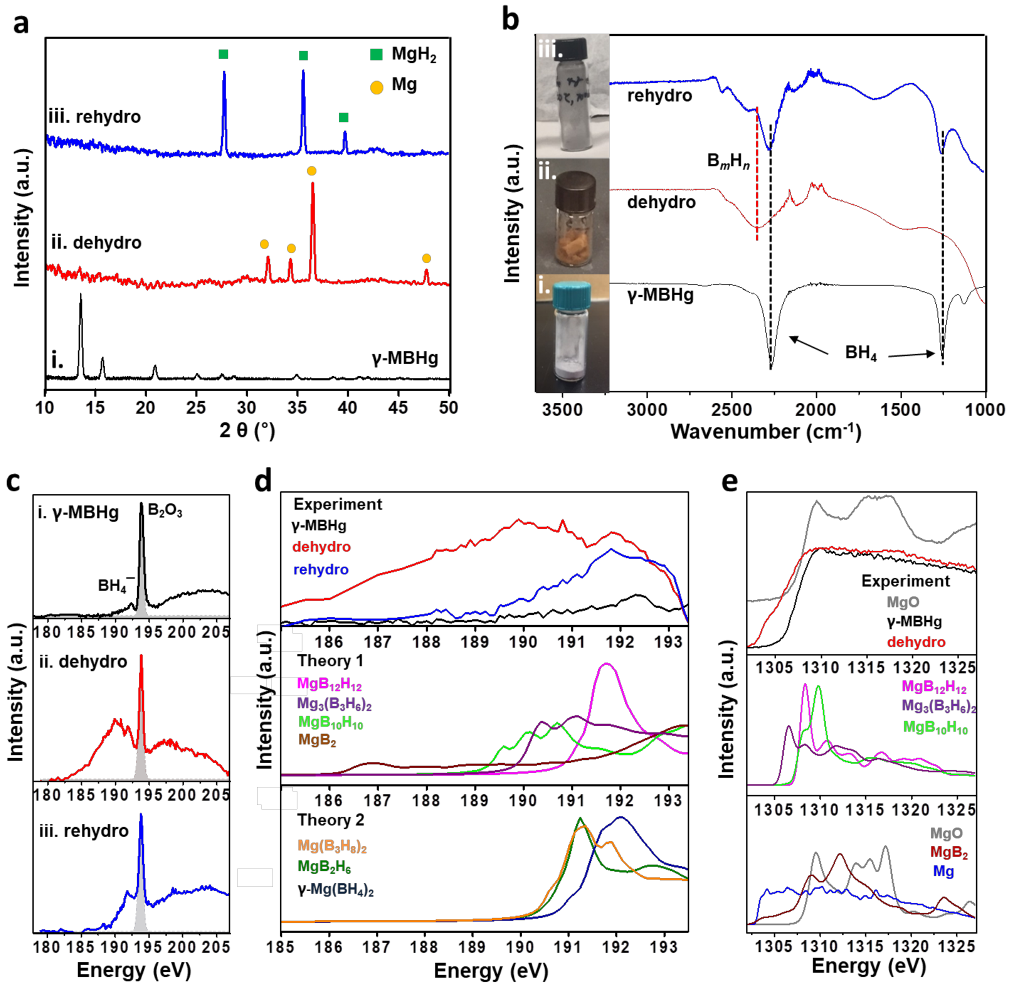

Figure 6. Experimental characterization of the de- and rehydrogenation products in γ-MBHg; a) Powder X-ray diffraction patterns, (b) FT-IR spectra, and (c) boron K-edge XAS spectra of (i) as-synthesized (black), (ii) dehydrogenated (red), (iii) rehydrogenated (blue) MBHg; d) Boron K-edge spectra were modified by subtracting boron oxide (B_2O_3) from original spectra (c) to enhance the signals of B_mH_n species. d) Simulated boron K-edge XAS spectra of expected dehydrogenated (Theory 1) and rehydrogenated (Theory 2) products. e) Mg K-edge XAS spectra of as-synthesized (black), dehydrogenated (red) MBHg, compared with reference MgO sample. Simulated Mg K-edge XAS spectra of expected dehydrogenated products (middle and bottom panels).

The dehydrogenation/rehydrogenation pathway in MBHg was further studied *via* powder X-ray diffraction, Fourier transform infrared (FT-IR) spectroscopy, X-ray absorption spectroscopy (XAS), and TEM. Powder X-ray diffraction data revealed that all phases of MBHg undergo similar transformations after hydrogen release and uptake and that magnesium and magnesium hydride are the only crystalline products of dehydrogenation and rehydrogenation, respectively (Figures 6a and Supporting Information,

Figure S14). While these data provide considerable information on the crystalline phases present, understanding the nature of amorphous products is also crucial, and thus we turned to spectroscopic techniques to better characterize potential amorphous products. The IR spectrum of as-synthesized γ-MBHg (black curve, Figure 6b) features sharp stretching and bending modes of BH_4^- at 2275 and 1252 cm^{-1}, respectively.[10] The intensities of these bands decrease following dehydrogenation, and a new broad peak grows in at ~2330 cm^{-1}, which may belong to newly formed borane compounds (red curve, Figure 6b). Upon rehydrogenation, the sharp BH_4^- peaks at 2275 and 1252 cm^{-1} appear again (blue curve, Figure 6b), suggesting that borohydride formation is partially reversible. Similar results were also observed in the IR spectra of α- and β-MBHg (Supporting Information, Figure S15). As shown in the inset to Figure 6b, the as-synthesized and rehydrogenated γ-MBHg samples also exhibit similar gray colors, while dehydrogenated γ-MBHg is a brown color indicative of $[B_mH_n]^{x-}$ containing compounds. Most prior reports have suggested that decomposition of MBH may occur through a polymerization process involving various $[B_mH_n]^{x-}$ monomers, mainly $B_{12}H_{12}^{2-}$;[37] however, these studies are inconclusive due to the lack of known spectra of the proposed compounds.

To further understand the de- and rehydrogenation pathway in MBHg, we also simulated XAS spectra and collected corresponding experimental data (see Figure 6c,d for γ-MBHg). First principles calculations were used to simulate spectra for $MgB_{10}H_{10}$, $Mg_3(B_3H_6)_2$, MgB_2H_6, MgB_2, $MgB_{12}H_{12}$, $Mg(BH_4)_2$, and $Mg(B_3H_8)_2$ (Figure 6d, lower two panels) to aid in the interpretation of major experimental features in the XAS spectra that possibly correspond to amorphous borane and/or Mg-polyborane compounds. The dominant boron K-edge spectroscopic signature at ~194 eV is primarily attributed to boron oxide formation, while the low energy feature around 192 eV is ascribed to BH_4^-, based on the simulated spectra for bulk γ-$Mg(BH_4)_2$. The experimental boron K-edge total fluorescence yield spectrum of dehydrogenated γ-MBHg is significantly broadened around 190 eV, indicating various $[B_mH_n]^{x-}$ species, including $MgB_{10}H_{10}$, $MgB_{12}H_{12}$, MgB_2, and $Mg_3(B_3H_6)_2$ (c.f. the simulated spectra in the middle panel of Figure 6d). These data support that dehydrogenation leads to a B:H ratio close to or smaller than 1:1. Once rehydrogenated, the sample may form $Mg(BH_4)_2$, $Mg(B_3H_8)_2$, and MgB_2H_6 (bottom panel, Figure 6d); indeed, $Mg_3(B_3H_6)_2$ is theorized to be a metastable intermediate which can be rehydrogenated back to $Mg(BH_4)_2$.[38] Although the signals of $[B_mH_n]^{x-}$ species are almost indistinguishable due to their chemical similarity, the combined computational and experimental analysis implies that our synthesized γ-MBHg follows multiple reaction pathways in both the dehydrogenation and rehydrogenation processes.

XAS measurements were also performed at the Mg K-edge to further investigate the chemical changes induced during the dehydrogenation (Figure 6e). X-ray absorption spectra for as-synthesized and dehyrogenated samples of γ-MBHg revealed a shift to lower energies upon dehydrogenation (~1306 *versus* ~1302 eV), as well as an increase in the intensity of the edge over the energy range 1302–1307 eV.

The spectral features generated upon dehydrogenation include contributions from $MgB_{10}H_{10}$, $MgB_{12}H_{12}$, $Mg_3(B_3H_6)_2$, MgB_2, and Mg, consistent with the results of the boron K-edge measurements. Finally, we note that the TEM images (Figure 7a) show well-preserved nanostructures and the absence of agglomeration after de- and rehydrogenation. Importantly, the as-synthesized γ-MBHg composite also shows better oxidative stability compared to pure γ-MBH, which might lead to larger amount of H_2 release in the rGO-supported system as less hydrogen would be consumed through oxidation[33] (see Figure 7b and Supporting Information, Figure S16-S17). In addition, the sharp peak seen in the MgO spectrum (gray) at 1309 eV is not distinctly observed in the dehydrogenated sample (Figure 6e, low panel). To confirm the degree of oxidation we have examined the B K-edge XAS spectra of MBH with rGO and without rGO and compared the areas corresponding to BH_4 and B_2O_3 (Supporting Information, Figure S18). The fitting areas in of the peak corresponding to BH_4 at ~192 eV in MBH with rGO (0.073824) are larger than that of the BH_4 peak in MBH without rGO (0.057521). Additionally, the spectra related to B_2O_3 at ~194 eV have the opposite fitting areas in MBH with rGO (0.22993) and without rGO (0.4227).

We expect this atomically-thin rGO layer will play a critical role contributing to the favorable reversibility of metal borohydride de- and rehydrogenation reactions.

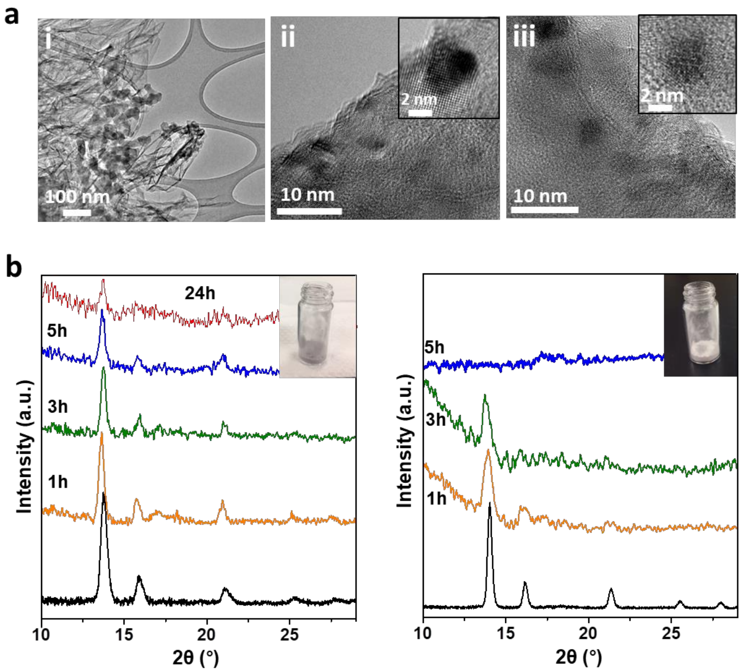

Figure 7. a) TEM images of (i) as-synthesized (black), (ii) dehydrogenated (red), (iii) rehydrogenated (blue) γ-MBHg. b) Air-exposed time-dependent powder X-ray diffractions spectra of γ-MBH with (left) and without (right) rGO.

Conclusion

In conclusion, we have demonstrated that the γ, β, and α phases of MBH can be selectively produced within reduced graphene oxide supports under mild conditions by carefully controlling the synthesis conditions. Experimental and theoretical analyses of the phase transformation mechanisms revealed that the γ-α phase mixture (sample **2**) is transformed into the thermodynamically stable α phase with increasing temperature. In contrast, the phase behavior of the as-synthesized pure γ phase (sample **1**) is governed by the preferred nucleation kinetics of the metastable β phase above 150 °C, possibly as a result of the energy penalty of directly nucleating the α phase in the γ phase. Our MBHg composites also exhibit potential cyclability, although the amount of recharged hydrogen is limited. Investigation of de- and rehydrogenated MBHg samples revealed evidence for corresponding chemical pathways, important microstructural features, as well as improved structural stability and oxidation resistivity, suggesting the potential reversibility and promising cycling performances of phase-controlled complex metal borohydrides supported by rGO.

Methods

Synthesis of $Mg(BH_4)_2$/rGO. All chemicals were stored in an Ar glove box when not in use. All processes were carried out in an Ar glovebox except for centrifugation. Reduced graphene oxide (rGO) was purchased from ACS materials and used without further purification, and 1 M $Mg(C_4H_9)_2$ in heptane and 2M $BH_3 \cdot S(CH_3)_2$ were purchased from Sigma Aldrich. First, rGO (4 mg) was dispersed in anhydrous toluene (8 mL) under Ar and sonicated for 40 min. The rGO solution was added to 10 mL of 1 M $Mg(C_4H_9)_2$ in heptane, which was then diluted with 16 mL of anhydrous toluene. The reaction mixture was allowed to stir for 30 min. The resulting rGO/$Mg(C_4H_9)_2$ solution was added to 20 mmol of $BH_3 \cdot S(CH_3)_2$ in varying amounts of anhydrous toluene, resulting in the formation of a gray precipitate. The solution was allowed to stir under Ar overnight. After the reaction, the solution was centrifuged (6,000 rpm, 20 min), and the supernatant was decanted to remove excess toluene and precursors. The white precipitate was washed 3 times with anhydrous toluene and subsequently dried either under vacuum at 4 Torr for 3 min, or under Ar for 1 day, producing sample **1** and sample **2**, respectively. The prepared samples were then heated between of 60 and 200 °C under vacuum at 2 Torr for 7 hours.

Characterization. Fourier transform infrared (FTIR) spectra were obtained with an Agilent Cary-630 spectrometer, with an attenuated total reflectance module containing a diamond crystal, located inside an argon glovebox to prevent exposure to air. PXRD patterns were acquired with a Bruker AXS D8 Discover GADDS X-Ray Diffractometer, using Cu and Co Kα radiation. High-resolution synchrotron X-ray powder diffraction data were subsequently collected at beamline 12.2.2 at the Advanced Light Source (ALS), Lawrence Berkeley National Laboratory. Samples were loaded into 1.0 mm glass capillaries inside a glovebox under an Ar atmosphere and sealed with clay. Analysis of powder X-ray diffraction patterns was performed using TOPAS-Academic v4.1. Indexing of the powder X-ray diffraction patterns of samples $Mg(BH_4)_2 \cdot xS(CH_3)_2$ indicated unit cells consistent with that previous reports. Hydrogen desorption measurement was performed using a HyEnergy PCT Pro-2000. The high-pressure hydrogenation experiments were performed in a custom pressure system with an Aminco compressor and a vessel made from Hi-Pressure 316 stainless steel components. Samples were loaded into holders with frits on one end that fit inside the vessel so that up to four could be loaded at a time. Thermogravimetric Analysis was measured using a Mettler-Toledo TGA/DSC 1 STARe. 2-5mg of samples were filled inside a glovebox in a pre-weighted aluminum crucible. The samples were heated with a ramp of 5 K min^{-1} under an argon flow of 20 ccm min^{-1}. Gas Analysis was done on a custom-built set-up, equipped with a turbo molecular pump (Agilent V70D, 75000 rpm) and a Stanford Research Systems CIS 200 closed ion source mass spectrometer with a sample range from 1-200 atomic mass units. Soft X-ray absorption spectroscopy measurements at Boron and Magnesium K-edges were carried out at beamlines 7.3.1 and 8.0.1.1 at the Advanced Light Source (ALS), Lawrence Berkeley National Laboratory. The energy resolutions for the Boron and Magnesium K-edges were set to 0.1 and 1 eV, respectively. All XAS spectra were normalized to incident photon flux and energy calibrated to known reference samples. Samples were prepared in Ar-glovebox (<0.1 ppm H_2O and O_2) and transferred to experimental XAS chamber with UHV compatible transfer kit without exposing to air at any time. XAS spectra were recorded simultaneously with the experimental chamber pressure $>1\times10^{-9}$ Torr.

Details of the phase nucleation modeling for $Mg(BH_4)_2$ polymorphic phases

Derivation of Gibbs free energies for the α, β, and γ polymorphs. For Gibbs free energies of relevant polymorphic phases, we relied on the existing CALPHAD (CALculation of PHAse Diagrams) databases.[39] In particular, we used the free energy functions (G_α and G_γ in J/mol) in the database for the α and γ phases given as the following [39]:

$$G_\alpha = G(hcp - Mg) - 222624.9 + 158.46145 \cdot T - 35.22138 \cdot T \cdot \ln(T) - 0.035975 \cdot T^2,$$
$$G_\gamma = G_\alpha + 3900,$$

where $G(hcp - Mg)$ is the Gibbs free energy of pure *hcp*-Mg with respect to the enthalpy (H^{SER}) at 298.15 K and 1b ar as Standard Element Reference (SER)[40] and T is the temperature. However, for the β phase, we calibrated the free energy function in a way that all three free energy curves well reproduce the characterized phase transition temperatures (*i.e.*, $T_{\gamma\to\beta}$~150°C and $T_{\alpha\to\beta}$~184°C for $\gamma \to \beta$ and $\alpha \to \beta$ phase transitions, respectively). The calibrated function G_β for the β phase is given as:

$$G_\beta = k_0 \cdot G_\alpha + k_1 \cdot (12954.437 - 26.4266 \cdot T),$$

where k_0 and k_1 are calibration factors which are identified to be 1.012 and 3.83, respectively, to reproduce the transition temperatures as shown in Figure 3a of the main text. Note that the original free energy functions in the database by Pinatel *et al*.[39] do not reproduce the relevant phase transition temperatures to our experimental observations. Therefore, our calibrated free energy functions may allow us to construct the kinetic phase nucleation model (see below) incorporating appropriate thermodynamic driving forces, which can explain the phase transformation behavior observed in our experiments.

DFT calculation for estimating the polymorphic phase boundary energy. We have estimated the energy of polymorphic phase boundaries using density functional theory (DFT) calculations. Explicit modeling of the phase boundaries between $Mg(BH_4)_2$ polymorphs is extremely challenging due to the inherent structural complexity the polymorphs and the phase boundaries arising from lattice mismatch, lattice misorientation, as well as the local orientations and arrangements of BH_4^- anions. However, the energy variation of α, β, and γ-$Mg(BH_4)_2$ polymorphs (~0.16 eV) is much smaller than is cohesive energy (~1.37 eV)—a condensation driving force from an isolated molecule to bulk crystalline[41], implying that the local clustering and covalent bonds between Mg-BH_4 is more significant for stabilizing the $Mg(BH_4)_2$ phase than the long-range order. Moreover, at the phase boundary where the symmetry is broken, the Mg^{2+} and BH_4^- units may rearrange and reorient to stabilize the phase boundary. Thus, it is reasonable to assume that the $Mg(BH_4)_2$ polymorphic phase boundaries are coherent and the energies of the α/β, α/γ, and β/γ boundaries are comparable. To this end, we approximated the $Mg(BH_4)_2$ polymorphic phase boundary energies to the antiphase boundary (APB) in the β'-$Mg(BH_4)_2$ phase. The β' phase is a disordered β phase, and J.-H. Her *et al*. reported the origin of disorder in the β' phase as the antiphase boundary in the *a*-axis direction.[42] The local arrangements and site symmetries of Mg^{2+} and BH_4^- units in the β' phase are similar to those in the β phase, and hence the energy difference between β and β' phases dominantly arises from the antiphase boundary. We computed the energy of β and β' phases using the generalized gradient approximation (GGA) functional developed by Perdew, Burke, and Ernzerhof (PBE)[43] and projected augmented wave (PAW) approach[44] as built in the Vienna *Ab Initio* Simulation Package (VASP).[45] The calculated energy difference between β and β' phases is 0.677 eV per unitcell containing two antiphase boundaries, while the antiphase boundary area is 215 Å^2. The resulting antiphase boundary energy of 1.6 meV/Å^2, corresponding to 25.3 mJ/m^2. This energy was used to approximate the ranges of interfacial energies, $\sigma_{\alpha\gamma}$ and $\sigma_{\beta\gamma}$, for our nucleation kinetic modeling presented in Figure 3.

Calculation of nucleation barriers and critical nuclei size. The properties of a critical nucleus (including size and activation energy barrier for nucleation) were calculated as a function of temperature for the β phase during $\gamma \rightarrow \beta$ transition and the α phase during $\gamma \rightarrow \alpha$ transition using the classical nucleation theory (CNT). Taking $\gamma \rightarrow \alpha$ transition as an example, the radius of a spherical critical nucleus of the α phase, $r^*_{\gamma\alpha}$, is given by:

$$r^*_{\gamma\alpha} = \frac{2\sigma_{\gamma\alpha}}{\Delta G_m^{\gamma\alpha}}$$

where $\sigma_{\gamma\alpha}$ is the α/γ interface energy and $\Delta G_m^{\gamma\alpha}$ the chemical driving force for nucleation. The activation energy barrier for nucleation is given by:

$$\Delta G^*_{\gamma\alpha} = \frac{16\pi\sigma_{\gamma\alpha}^3}{3\left(\Delta G_m^{\gamma\alpha}\right)^2}$$

For the $\gamma \rightarrow \beta$ transition, the critical nucleus radius $r^*_{\gamma\alpha}$ and the activation energy barrier for nucleation $\Delta G^*_{\gamma\beta}$ are calculated in the same way. Both $\Delta G_m^{\gamma\alpha}$ and $\Delta G_m^{\gamma\beta}$ as a function of temperature are informed by the CALPHAD-derived free energies as explained above. The interfacial energies $\sigma_{\gamma\alpha}$ and $\sigma_{\gamma\beta}$ are estimated based on the computed antiphase boundary (or stacking fault) energy above, $25 - 40\ \mathrm{mJ/m^2}$. Accordingly, for each temperature, both $\sigma_{\gamma\alpha}$ and $\sigma_{\gamma\beta}$ are varied within $10 - 50\ \mathrm{mJ/m^2}$. The corresponding activation energy barriers are calculated and compared to evaluate the propensity of relevant phase transformations at each temperature.

X-ray absorption spectroscopy simulations

The X-ray absorption near edge structures for B K-edge were simulated using the Vienna *Ab*-Initio Simulation Package (VASP).[46-49] A plane-wave cutoff of 600 eV was used and the k-point sampling was chosen for each material such that the density of k-points was > 64000 per Å^3. Perdew–Burke–Ernzerhof (PBE) type generalized gradient approximation was used to approximate the exchange-correlation energy in DFT.[50] PAW pseudopotentials chosen from the VASP library were used for all ground state atoms and a modified pseudopotential containing a core-hole at the 1s level was used for the excited atom.[51] The calculated dipole transition amplitude from the initial to the final state was further convoluted using a Gaussian function with a width of 0.2 eV to obtain a continuous smooth spectrum. We selected the crystal structures of all intermediates from those published in the literature.[52-56] To account for thermal fluctuations of the structures at room temperature, *ab initio* molecular dynamic simulations (AIMD) were performed at 298.15 K with a 0.5 fs time step. Over 1000 uncorrelated B environments were chosen in time and space from the AIMD trajectory to compute an ensemble averaged X-ray absorption spectrum, as shown in Figure 6d of the main text. The calculated B K-edge spectra were properly internally aligned according to the alignment scheme as introduced in Ref. 57 To compare with the experiment, a constant shift as referencing to γ-$Mg(BH_4)_2$ was applied to all computed B K-edge spectra.

The Mg K-edge XAS spectra were computed using the Quantum ESPRESSO source code package with the Shirley reduced basis set for efficient k-point sampling.[58,59] Ultrasoft pseudopotentials were used for all atoms, expect for the excited atom, where a modified pseudopotential with a core hole was used.[60] The final state was approximated within the excited core-hole approach as discussed in Ref.61. The PBE-GGA approximation was used to compute the exchange-correlation functional in DFT and sufficient k-point sampling was used in all calculations to ensure numerical convergence. The spectra presented in Figure 6e of the main text are based on single static structures optimized using DFT and each computed spectrum was further convoluted by a Gaussian broadening of 0.5 eV. The Mg K-edge XAS data for Mg metal and MgO are reproduced from Ref.62.

Associated Content

Supporting Information

The Supporting Information is available free of charge on the ACS Publications Website at DOI:

Additional PXRD, TEM, STEM-EDS, Mass spectra, FT-IR spectra, thermogravimetric analysis, XAS spectra and hydrogen desorption characterization (PDF)

Notes

The authors declare no competing financial interest.

Acknowledgements: Work at the Molecular Foundry was supported by the Office of Science, Office of Basic Energy Sciences, of the U.S. Department of Energy under Contract No. DE-AC02-05CH11231. We thank Dr. Andrew Doran at the Advanced Light Source (ALS) for powder X-ray diffraction support. Part of the work was performed under the auspices of the DOE by Lawrence Livermore National Laboratory (LLNL) under Contract DE-AC52-07NA27344. Computing support came from the LLNL Institutional Computing Grand Challenge program. Sandia National Laboratories is a multi-mission laboratory managed and operated by National Technology and Engineering Solutions of Sandia, LLC, a wholly owned subsidiary of Honeywell International, Inc., for the U.S. Department of Energy's National Nuclear Security Administration under contract DE-NA-0003525. The materials are based on work supported by the Department of Energy (DOE) through Hydrogen Materials Advanced Research Consortium (HyMARC), established as part of the Energy Materials Network and funded by the U.S. Department of Energy, Office of Energy Efficiency and Renewable Energy, Fuel Cell Technologies Office (Contract

Number DE-AC02-05CH11231, DE-AC52-07NA27344, and DE-NA-0003525). This paper describes objective technical results and analysis. Any subjective views or opinions that might be expressed in the paper do not necessarily represent the views of the U.S. Department of Energy or the United States Government. We thank Dr. Katie R. Meihaus for editorial assistance.

References

1. Midilli, A.; Ay, M.; Dincer, I.; Rosen, M. On hydrogen and hydrogen energy strategies: I: current status and needs. *Renew. Sustain. Energy Rev.* **2005,** *9*, 255-271.
2. Schlapbach, L., Technology: Hydrogen-fuelled vehicles. *Nature* **2009,** *460*, 809.
3. Najjar, Y. S. Hydrogen safety: The road toward green technology. *Int. J. Hydrog. Energy* **2013,** *38*, 10716-10728.
4. Preuster, P.; Alekseev, A.; Wasserscheid, P. Hydrogen storage technologies for future energy systems. *Annu. Rev. Chem. Biomol* **2017,** *8*, 445-471.
5. Qiu, S.; Chu, H.; Zou, Y.; Xiang, C.; Xu, F.; Sun, L. Light metal borohydrides/amides combined hydrogen storage systems: composition, structure and properties. *J. Mater. Chem. A* **2017,** *5*, 25112-25130.
6. Li, H.-W.; Yan, Y.; Orimo, S.-i.; Züttel, A.; Jensen, C. M. Recent progress in metal borohydrides for hydrogen storage. *Energies* **2011,** *4*, 185-214.
7. Schneemann, A.; White, J. L.; Kang, S.; Jeong, S.; Wan, L. F.; Cho, E. S.; Heo, T. W.; Prendergast, D.; Urban, J. J.; Wood, B. C. Nanostructured metal hydrides for hydrogen storage. *Chem. Rev.* **2018,** *118*, 10775-10839.
8. Černý, R.; Filinchuk, Y.; Hagemann, H.; Yvon, K. Magnesium borohydride: synthesis and crystal structure. *Angew. Chem.* **2007,** *119*, 5867-5869.
9. Soloveichik, G. L.; Gao, Y.; Rijssenbeek, J.; Andrus, M.; Kniajanski, S.; Bowman Jr, R. C.; Hwang, S.-J.; Zhao, J.-C. Magnesium borohydride as a hydrogen storage material: Properties and dehydrogenation pathway of unsolvated $Mg(BH_4)_2$. *Int. J. Hydrog. Energy* **2009,** *34*, 916-928.
10. Zavorotynska, O.; El-Kharbachi, A.; Deledda, S.; Hauback, B. C. Recent progress in magnesium borohydride $Mg(BH_4)_2$: Fundamentals and applications for energy storage. *Int. J. Hydrog. Energy* **2016,** *41*, 14387-14403.
11. Chłopek, K.; Frommen, C.; Léon, A.; Zabara, O.; Fichtner, M. Synthesis and properties of magnesium tetrahydroborate, $Mg(BH_4)_2$. *J.Mater.Chem.* **2007,** *17*, 3496-3503.
12. Riktor, M.; Sørby, M.; Chłopek, K.; Fichtner, M.; Buchter, F.; Züttel, A.; Hauback, B., *In situ* synchrotron diffraction studies of phase transitions and thermal decomposition of $Mg(BH_4)_2$ and Ca $(BH_4)_2$. *J.Mater.Chem.* **2007,** *17*, 4939-4942.
13. Her, J.-H.; Stephens, P. W.; Gao, Y.; Soloveichik, G. L.; Rijssenbeek, J.; Andrus, M.; Zhao, J.-C. Structure of unsolvated magnesium borohydride $Mg(BH_4)_2$. *Acta Crystallogr. B Struct. Sci.* **2007,** *63*, 561-568.
14. Ozolins, V.; Majzoub, E.; Wolverton, C. First-principles prediction of a ground state crystal structure of magnesium borohydride. *Phys. Rev. Lett.* **2008,** *100*, 135501.
15. Setten, M. J. v.; Wijs, G. A. d.; Fichtner, M.; Brocks, G. A density functional study of α-$Mg(BH_4)_2$. *Chem. Mater.* **2008,** *20*, 4952-4956.
16. Filinchuk, Y.; Richter, B.; Jensen, T. R.; Dmitriev, V.; Chernyshov, D.; Hagemann, H. Porous and dense magnesium borohydride frameworks: synthesis, stability, and reversible absorption of guest species. *Angew. Chem.* **2011,** *123*, 11358-11362.
17. David, W.; Callear, S.; Jones, M.; Aeberhard, P.; Culligan, S.; Pohl, A.; Johnson, S.; Ryan, K.; Parker, J.; Edwards, P. The structure, thermal properties and phase transformations of the cubic polymorph of magnesium tetrahydroborate. *Phys. Chem. Chem. Phys.* **2012,** *14*, 11800-11807.
18. Paskevicius, M.; Pitt, M. P.; Webb, C. J.; Sheppard, D. A.; Filsø, U.; Gray, E. M.; Buckley, C. E. *In-situ* X-ray diffraction study of γ-$Mg(BH_4)_2$ decomposition. *J. Phys. Chem. C* **2012,** *116*, 15231-15240.
19. Paskevicius, M.; Jepsen, L. H.; Schouwink, P.; Černý, R.; Ravnsbæk, D. B.; Filinchuk, Y.; Dornheim, M.; Besenbacher, F.; Jensen, T. R. Metal borohydrides and derivatives–synthesis, structure and properties. *Chem. Soc. Rev.* **2017,** *46*, 1565-1634.
20. Pinatel, E. R.; Albanese, E.; Civalleri, B.; Baricco, M. Thermodynamic modelling of $Mg(BH_4)_2$. *J. Alloys Comp.* **2015,** *645*, S64-S68.

21. Caputo, R.; Tekin, A.; Sikora, W.; Züttel, A. First-principles determination of the ground-state structure of $Mg(BH_4)_2$. *Chem. Phys. Lett.* **2009,** *480*, 203-209.
22. Voss, J.; Hummelshøj, J. S.; Łodziana, Z.; Vegge, T. Structural stability and decomposition of $Mg(BH_4)_2$ isomorphs—an *ab* initio free energy study. *J. Condens. Matter Phys.* **2008,** *21*, 012203.
23. Huot, J.; Ravnsbæk, D. B.; Zhang, J.; Cuevas, F.; Latroche, M.; Jensen, T. R. Mechanochemical synthesis of hydrogen storage materials. *Prog. Mater. Sci.* **2013,** *58*, 30-75.
24. Matsunaga, T.; Buchter, F.; Miwa, K.; Towata, S.; Orimo, S.; Züttel, A. Magnesium borohydride: A new hydrogen storage material. *Renewa. Energy* **2008,** *33*, 193-196.
25. Zhang, Z.; Zhang, S.; Wang, H.; Liu, J.; Zhu, M. Feasibility study of the direct synthesis of Mg $(BH_4)_2$ complex hydrides by mechanical milling. *J. Alloys Comp.* **2010,** *505*, 717-721.
26. Tumanov, N. A.; Safin, D. A.; Richter, B.; Łodziana, Z.; Jensen, T. R.; Garcia, Y.; Filinchuk, Y. Challenges in the synthetic routes to $Mn(BH_4)_2$: insight into intermediate compounds. *Dalton Trans.* **2015,** *44*, 6571-6580.
27. Zhang, Z.; Luo, F.; Wang, H.; Liu, J.; Zhu, M. Direct synthesis and hydrogen storage characteristics of Mg–B–H compounds. *Int. J. Hydrog. Energy* **2012,** *37*, 926-931.
28. Severa, G.; Rönnebro, E.; Jensen, C. M. Direct hydrogenation of magnesium boride to magnesium borohydride: demonstration of> 11 weight percent reversible hydrogen storage. *Chem. Commun.* **2010,** *46*, 421-423.
29. Soloveichik, G. L.; Andrus, M.; Gao, Y.; Zhao, J.-C.; Kniajanski, S. Magnesium borohydride as a hydrogen storage material: synthesis of unsolvated $Mg(BH_4)_2$. *Int. J. Hydrog. Energy* **2009,** *34*, 2144-2152.
30. Hagemann, H.; Černý, R. Synthetic approaches to inorganic borohydrides. *Dalton Trans.***2010,** *39*, 6006-6012.
31. Bateni, A.; Scherpe, S.; Acar, S.; Somer, M. Novel approach for synthesis of Magnesium Borohydride, $Mg(BH_4)_2$. *Energy Procedia* **2012,** *29*, 26-33.
32. Filinchuk, Y.; Cerny, R.; Hagemann, H. Insight into $Mg(BH_4)_2$ with synchrotron X-ray diffraction: structure revision, crystal chemistry, and anomalous thermal expansion. *Chem. Mat.* **2009,** *21* , 925-933.
33. Cho, E. S.; Ruminski, A. M.; Aloni, S.; Liu, Y.-S.; Guo, J.; Urban, J. J. Graphene oxide/metal nanocrystal multilaminates as the atomic limit for safe and selective hydrogen storage. *Nat. Commun.* **2016,** *7*, 10804.
34. Zanella, P.; Crociani, L.; Masciocchi, N.; Giunchi, G. Facile high-yield synthesis of pure, crystalline Mg $(BH_4)_2$. *Inorg. Chem.* **2007,** *46*, 9039-9041.
35. Porter, D. A.; Easterling, K. E.; Sherif, M. *Phase Transformations in Metals and Alloys, (Revised Reprint)*. CRC press: 2009.
36. Heo, T. W.; Tang, M.; Chen, L. Q.; Wood, B. C. Defects, entropy, and the stabilization of alternative phase boundary orientations in battery electrode particles. *Adv. Energy Mater.* **2016,** *6*, 1501759.
37. Newhouse, R. J.; Stavila, V.; Hwang, S.-J.; Klebanoff, L. E.; Zhang, J. Z. Reversibility and improved hydrogen release of magnesium borohydride. *J. Phys. Chem. C* **2010,** *114*, 5224-5232.
38. Zhang, Y.; Majzoub, E.; Ozoliņš, V.; Wolverton, C. Theoretical prediction of metastable intermediates in the decomposition of $Mg(BH_4)_2$. *J. Phys. Chem. C* **2012,** *116*, 10522-10528.
39. Pinatel, E.R.; Albanese, E.; Civalleri, B.; Baricco, M. Thermodynamic Modelling of $Mg(BH_4)_2$. *J. Alloys Comp.* **2015**, 645, S64-S68.
40. Dinsdale, A.T., *CALPHAD*, **1991**, *15*, 317-425
41. Kang, S; Heo, T. W.; Allendorf, M. D.; Wood, B. C. Morphology-Dependent Stability of Complex Metal Hydrides and Their Intermediates Using First-Principles Calculations. *ChemPhysChem* **2019**, *20*, 1340-1347.
42. Her, J. H.; Stephens, P. W.; Gao, Y.; Soloveichik, G. L.; Rijssenbeek, J.; Andrusb, M.; Zhao, J. C. Structure of Unsolvated Magnesium Borohydride $Mg(BH_4)_2$. *Acta Crystallogr.* **2007**, *B63*, 561–568.

43. Perdew, J. P.; Burke, K.; Ernzerhof, M. Generalized Gradient Approximation Made Simple. *Phys. Rev. Lett.* **1996**, *77*, 3865–3868.

44. Blöchl, P. E. Projector Augmented-Wave Method. *Phys. Rev. B* **1994**, *50*, 17953–17979.

45. Kresse, G.; Furthmüller, J. Efficient Iterative Schemes for *Ab* initio Total-Energy Calculations Using a Plane-Wave Basis Set. *Phys. Rev. B*, **1996**, *54*, 11169–11186.

46. Kresse, G.; Hafner, *Ab* initio Molecular Dynamics for Liquid Metals. J. *Phys. Rev. B: Condens. Matter Mater. Phys.,* **1993**, *47*, 558–561.

47. Kresse, G.; Hafner, J. *Ab* initio Molecular-Dynamics Simulation of The Liquid-Metal Amorphous-Semiconductor Transition in Germanium. *Phys. Rev. B: Condens. Matter Mater. Phys.*, **1994**, *49*, 14251–14269.

48. Kresse, G.; Furthmller, J. Efficiency of *Ab*-initio Total Energy Calculations for Metals and Semiconductors Using a Plane-Wave Basis Set. *Comput. Mater. Sci.,* **1996**, *6*, 15–50.

49. Kresse, G.; Joubert, D. From Ultrasoft Pseudopotentials to The Projector Augmented-Wave Method. *Phys. Rev. B: Condens. Matter Mater. Phys.*, **1999**, *59*, 1758–1775.

50. Perdew, J. P.; Burke, K. Comparison Shopping for a Gradient-Corrected Density Functional. *Int. J. Quantum Chem.,* **1996**, *57*, 309–319.

51. Ray, K. G.; Klebanoff, L. E.; Lee, J. R. I.; Stavila, V. ; Heo, T. W.; Shea, P.; Baker, A. A.; Kang, S.; Bagge-Hansen, M.; Liu, Y.-S.; White, J. L.; Wood, B. C. Elucidating the mechanism of MgB_2 initial hydrogenation via a combined experimental–theoretical study. *Phys. Chem. Chem. Phys.*, **2017**, *19*, 22646-22658.

52. Jain, A.; Ong, S.P.; Hautier, G.; Chen, W.; Richards, W.D.; Dacek, S.; Cholia, S.; Gunter, D.; Skinner, D.; Ceder, G.; Persson, K.A. The Materials Project: A materials genome approach to accelerating materials innovation. *APL Materials*, **2013**, *1*, 011002.

53.Saal, J. E.; Kirklin, S.; Aykol, M.; Meredig, B.; Wolverton, C. Materials Design and Discovery with High-Throughput Density Functional Theory: The Open Quantum Materials Database (OQMD). *JOM*, **2013**, *65*, 1501–1509.

54. Kirklin, S.; Saal, J.E.; Meredig, B.; Thompson, A.; Doak, J.W.; Aykol, M.; Rühl, S. ;Wolverton, C. The Open Quantum Materials Database (OQMD): assessing the accuracy of DFT formation energies. *npj Computational Materials*, **2015**, *1*, 15010.

55. Ozolins, V.; Majzoub, E. H.; Wolverton, C. First-Principles Prediction of Thermodynamically Reversible Hydrogen Storage Reactions in the Li-Mg-Ca-B-H System. *J. Am. Chem. Soc.*, **2008**, *131*, 230–237.

56. Zhang, Y.; Majzoub, E.; Ozolins, V.; Wolverton, C. Theoretical Prediction of Metastable Intermediates in the Decomposition of $Mg(BH_4)_2$. *J. Phys. Chem. C*, **2012**, *116*, 10522–10528.

57. England, A. H.; Duffin, A. M.; Schwartz, C. P.; Uejio, J. S.; Prendergast, D.; Saykally, R. On the Hydration and Hydrolysis of Carbon Sioxide. *J. Chem. Phys. Lett.* **2011**, *514*, 187–195.

58. Giannozzi, P.; Baroni, S.; Bonini, N.; Calandra, M.; Car, R.; Cavazzoni, C.; Ceresoli, D.; Chiarotti, G. L.; Cococcioni, M.; Dabo, I.; Dal Corso, A.; de Gironcoli, S.; Fabris, S.; Fratesi, G.; Gebauer, R.; Gerstmann, U.; Gougoussis, C.; Kokalj, A.; Lazzeri, M.; Martin-Samos, L. *et al*. QUANTUM ESPRESSO: A Modular and Open-Source Software Project for Quantum Simulations of Materials. *J. Phys.: Condens. Matter*. **2009**, *21*, 395502 1–19.

59. Prendergast, D.; Louie, S. G. Bloch-State-Based Interpolation: An Efficient Generalization of The Shirley Approach to Interpolating Electronic Structure. *Phys. Rev. B* **2009**, *80*, 235126– 235126.

60. Vanderbilt, D. Soft Self-Consistent Pseudopotentials in A Generalized Eigenvalue Formalism. *Phys. Rev. B* **1990**, *41*, 7892–7895.

61. Prendergast, D.; Galli, G. X-Ray Absorption Spectra of Water from First Principles Calculations. *Phys. Rev. Lett.* **2006**, *96*, 215502 1–4.

62. Wan, L. F. ; Liu, Y.-S.; Cho, E. S.; Forster, J. D. ; Jeong, S. ; Wang, H.-T.; Urban, J. J. ; Guo, J. Prendergast, D. Atomically Thin Interfacial Suboxide Key to Hydrogen Storage Performance Enhancements of Magnesium Nanoparticles Encapsulated in Reduced Graphene Oxide. *Nano Lett*. **2017**, *17*, 540–545.

Table of Contents